ACS APPLIED NANO MATERIALS

www.acsanm.org Article

Electron-Deficient Au Nanoparticles Confined in Organic Molecular Cages for Catalytic Reduction of 4-Nitrophenol

Yali Liu,[#] Hongliang Dong,[#] Haowei Huang, Wei Zong, Yue-E Miao, Guanjie He, Ivan P. Parkin, Feili Lai,* and Tianxi Liu*

HPSTAR 1619-2022

Cite This: *ACS Appl. Nano Mater.* 2022, 5, 1276−1283 Read Online

ACCESS | Metrics & More | Article Recommendations | Supporting Information

ABSTRACT: Noble-metal nanoparticles are regarded as one of the most promising catalysts to reduce the organic pollutant 4-nitrophenol (4-NP). However, the inevitable agglomeration of noble-metal nanoparticles and their poor distributions in catalytic systems limit their performance. Here, we propose a strategy to encapsulate Au nanoparticles inside porous organic cages (POCs) of soluble RCC3 and stabilize the size of Au nanoparticles at ∼3.25 nm. Typically, the Au@RCC3 composite exhibits excellent 4-NP catalytic reduction performance, which is superior to the corresponding Au bulk catalyst and is also closely related to the size of Au nanoparticles. The normalized X-ray absorption near-edge structure (XANES) results indicate that the electron deficiency at the Au atoms in Au@RCC3 is due to the existence of the RCC3 cage, which is beneficial to accelerate the electron transfer from BH_4^- to 4-NP during the hydrogenation process. This is also shown by density functional theory (DFT), in which a low energy barrier of 1.03 eV exists for the Au_{12} cluster compared with 1.37 eV for the Au_{25} cluster. Therefore, the encapsulation of noble-metal nanoparticles with soluble POCs is an effective way to design and develop stable active catalysts rationally.

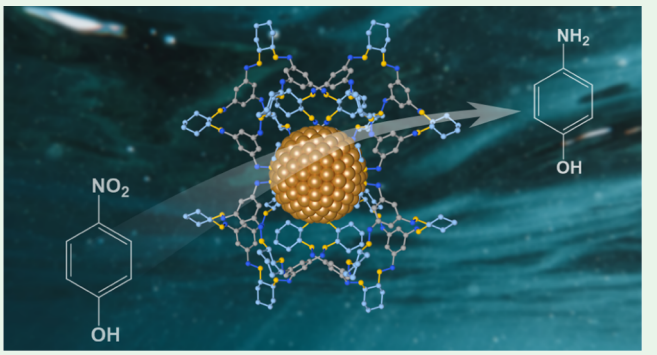

KEYWORDS: *porous organic cage, metal nanoparticle, organic catalysis, 4-nitrophenol, pollutant degradation*

1. INTRODUCTION

Nitrophenols are hazardous, nonbiodegradable, and toxic compounds that cause many human diseases.[1] As a typical nitro compound, 4-nitrophenol (4-NP) can be used as an intermediate in pesticides, dyes, and medicines.[2] Due to its high water solubility and excellent chemical stability, 4-NP is easily enriched in living organisms and stays in the environment for a considerable time, leading to severe ecological problems and causing toxic or carcinogenic effects on humans and animals.[3,4] As a result, it has been listed as one of the primary pollutants controlled by both China and the U.S. Environmental Protection Agencies (the concentration of 4-NP in water is not allowed to exceed 10 ng L^{-1}).[5] There is widespread attention on how to wisely and effectively remove 4-NP from wastewater.[6]

To date, various traditional methods have been developed to improve the efficiency of 4-NP removal from wastewater, such as adsorption,[7] photocatalytic degradation,[2] and oxidative degradation.[8] However, these methods often suffer from high investment costs and long operation times and are susceptible to secondary contamination. Recently, the reduction of 4-NP to the less toxic and biodegradable 4-aminophenol (4-AP) with $NaBH_4$ has been reported to be an effective method for treating 4-NP.[9] On the other hand, 4-AP is a widely used industrial material for preparing analgesic and antipyretic drugs, dyes, and antiseptic lubricants, which is of commercial importance.[3] Therefore, the reduction of 4-NP to 4-AP plays a significant role in environmental protection and industrial application. At the same time, the method has the advantages of a simple operation process, mild reaction conditions, and complete conversion of 4-NP to 4-AP without the formation of byproducts.[10−14] However, the reaction requires the addition of a catalyst to proceed. Therefore, it is of great significance to investigate catalysts that can be used for the effective degradation of 4-NP and the formation of 4-AP.

To date, various heterogeneous and nanostructured catalysts have been developed and designed to reduce 4-NP into 4-AP,[15−18] among which metal nanoparticles (MNPs) exhibit unique catalytic properties (especially in liquid phase systems) due to their high surface area-to-volume ratio and versatile electronic/geometric structures.[19−21] Generally, the key point

Received: November 13, 2021
Accepted: December 30, 2021
Published: January 12, 2022

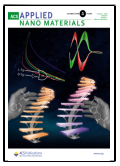

ACS Publications © 2022 American Chemical Society

to modulate the catalytic activities of MNPs is by reducing their sizes, regulating their nanoscale morphologies, and modulating their microstructures. However, due to the high surface energy of ultrafine MNPs, they very easily coalesce into large particles with the generation of blocked surfaces, which makes catalytic activity and long-term stability drop sharply. To maintain the ultrafine size of MNPs and make the active sites as accessible as possible, two possible strategies have been proposed: (1) to protect ultrafine MNPs using various stabilizers; however, these often prevent the diffusion of reactants to the MNPs, resulting in reduced catalytic activities,[22−24] and (2) to find suitable supports with a high specific surface area to anchor MNPs; however, this approach is still restricted by the weak affinities between the MNPs and supports.[25−27] Therefore, it is still a huge challenge to construct suitable MNP-support structures with both high stability and catalytic activity.

Since the discovery of organic molecular cages, the scientific community's research interest in these porous materials has steadily grown.[28−32] Compared with most three-dimensional porous open frames, the vast majority of porous organic cages (POCs) possess very unique properties, which means they can be well dissolved in common organic solvents, with good stability and dispersibility. On the other hand, their excellent solubilities enable them to be well composited with various materials, which broadens their applications (e.g., small molecule separation,[33−35] sensing,[36,37] molecular components of polymers,[38,39] and nanoparticle templates[40−46]). Due to the inherent porous behaviors and guest-accessible cavities in POCs, the encapsulation of various MNPs inside POCs is a promising approach to developing stable and active catalysts. By stabilizing MNPs in soluble and ultrasmall cages to construct MNPs@POC composites, thousands of ultrafine MNPs can be well confined in the cage cavities with a narrow size distribution, which could not only solve the problem of NP aggregation but also enhance the stability of the MNPs. As a result, the catalytic activity of MNPs@POC composites may be enhanced due to the isolated MNPs in the open and discrete cavities with abundant accessible metal active sites and high dispersibility in the solution.

In this study, we encapsulated a series of Au nanoparticles with POCs to reduce the size of the Au nanoparticles and facilitate the catalytic reduction reaction of 4-NP (vide infra). Taking the Au-5@RCC3 nanocatalyst as an example, its Au loading amount is 4.22 wt % with a particle size of ∼3.25 nm and uniform distribution. This nanomaterial exhibits enhanced catalytic performance compared to the Au bulk. The reasons for the enhanced catalysis in Au-5@RCC3 were unveiled by the X-ray absorption near-edge structure (XANES) technology and density functional theory (DFT) calculations. Specifically, when the Au nanoparticles are confined in the POCs, the Au nanoparticles will be lightly oxidized with the generation of electron deficiency in the Au atoms, leading to accelerated electron transfer from BH_4^- to 4-NP during hydrogenation, which boosted the catalytic performance.

2. EXPERIMENTAL SECTION

2.1. Materials. Except for 1,3,5-triformylbenzene (Zhengzhou Alpha Chemical Co. Ltd.), all other chemicals were purchased from Aladdin Reagent Co. Ltd. and used as received.

2.2. Synthesis of CC3. The synthesis of CC3 was carried out according to a previous method.[47] First, CH_2Cl_2 (5 mL) was slowly added to solid 1,3,5-triformylbenzene (0.25 g) at room temperature without stirring. Then, trifluoroacetic acid (5 μL) was added directly as a catalyst. Finally, a solution of (*R*,*R*)-1,2-diaminocyclohexane (0.25 g) in CH_2Cl_2 (5 mL) was added. The container of the mixed solution was covered and allowed to stand for 1 week. Crystals were grown on the side of the vessel, separated by filtration, washed with CH_3CH_2OH/CH_2Cl_2 (v/v, 95/5) solution, and dried under vacuum at 70 °C overnight.

2.3. Synthesis of RCC3. RCC3 was synthesized according to a previous method.[48] The imine cage of CC3 (926 mg) was dissolved in a $CH_3OH/CHCl_3$ mixture (v/v, 1/1, 50 mL) to form a clear solution. Then, $NaBH_4$ (1.0 g) was added to initiate the reaction, which was further stirred at room temperature for 12 h. After adding 2 mL of deionized water, the solution was stirred continuously for 12 h. The solvent was then removed under vacuum. The resulting solid was washed with $CHCl_3$ (2 × 50 mL), and then the $CHCl_3$ phase was washed with deionized water (2 × 100 mL). The $CHCl_3$ phase was dried using anhydrous $MgSO_4$ before being removed under vacuum. RCC3 was purified using the reversible reaction with acetone.[48] In a 100 mL flask, 400 mg of crude RCC3 was dissolved in 40 mL of acetone. The solution was covered and left to stand. Crystals started appearing on the wall of the flask after 30 min. Crystals (AT-RCC3) were collected after 24 h by filtration and then dissolved in 40 mL of $CH_3OH/CHCl_3$ mixture (v/v, 1/1) by continuous stirring. Deionized water (0.4 mL) was added to the solution, and the mixture was stirred for another 48 h. After the removal of the solvents, pure RCC3 was recovered.

2.4. Synthesis of Au@RCC3 Catalyst. Typically, 46 mg of purified RCC3 powder was stirred and dissolved in a CH_3OH/CH_2Cl_2 mixed solution (v/v, 1/2, 18 mL). Subsequently, different amounts of $AuCl_3$ CH_3OH solution (4 mg mL^{-1}, 860 μL, 600 μL, and 350 μL) were added to the mixed solution and stirred for 3 h to form a homogeneous solution. Then, CH_3OH solutions containing different amounts of the reducing agent of $NaBH_4$ (51, 36, and 21 mg) were immediately added to the solution under ice bath conditions and stirred for 3 h. After that, the products were removed from the solvent under vacuum, washed several times with deionized water, and vacuum-dried at 70 °C overnight to obtain Au-7@RCC3, Au-5@RCC3, and Au-3@RCC3 catalysts.

2.5. Procedure for the Reduction of 4-NP. The reduction of 4-NP by $NaBH_4$ was chosen as a model reaction to test the catalytic activity of Au@RCC3 catalysts under ambient conditions. Typically, 2.5 mg of $NaBH_4$ was added to 4 mL of 4-NP (0.1 mmol L^{-1}) in CH_3OH/CH_2Cl_2 mixed solution (v/v, 1/2). A large amount of gas was immediately generated in the solution, and the color of the solution changed from light yellow to bright yellow with the shift of the absorption peak from 317 to 400 nm. After there is no generated gas in the solution, 0.2 mg of Au@RCC3 was added to the above mixed solution. After introducing the catalyst, the bright yellow solution gradually faded as the reaction proceeded. The catalytic hydrogenation process was monitored by ultraviolet−visible (UV−vis) light measurements in the wavelength range of 250−500 nm. The rate constants for the reduction process were determined by measuring the change in the absorbance at λ = 400 nm as a function of reaction time.

2.6. Theoretical Calculation Details. To understand the reduction pathway of 4-NP, density functional theory (DFT) calculations were performed using the Vienna Ab initio Simulation Package (VASP).[49,50] The ion−electron interactions were depicted by projector augmented waves (PAW) and the exchange and correlation potential described by the revised function of Perdew, Burke, and Ernzerhof (revPBE)[51] based on the generalized gradient approximation (GGA). In this work, 3 × 3 × 3 gamma *k*-point grids were used to sample the Brillouin zone for the supercell structures. A cutoff energy of 500 eV was adopted. To avoid the interaction between neighboring slabs over the periodic boundary cell, the vacuum space was set to be at least 20 Å. The criteria of convergence were set to 1×10^{-5} eV and 0.01 eV $Å^{-1}$ for the self-consistent field (SCF) and ion steps, respectively.

https://doi.org/10.1021/acsanm.1c03859
ACS Appl. Nano Mater. 2022, 5, 1276−1283

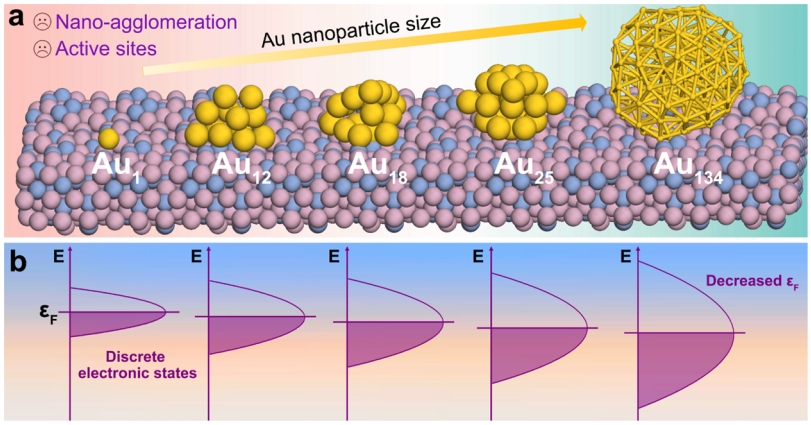

Figure 1. (a) Five representative Au models on a support from isolated Au atom (Au_1) and atomically dispersed nanoparticles (Au_{12}) to larger Au nanoparticles (Au_{18}, Au_{25}, and Au_{134}). (b) Schematic illustration for ideal density of states (DOS) of different Au models from isolated Au atom (left) to larger Au nanoparticles (right), where the DOS of the support was not taken into consideration.[38,45]

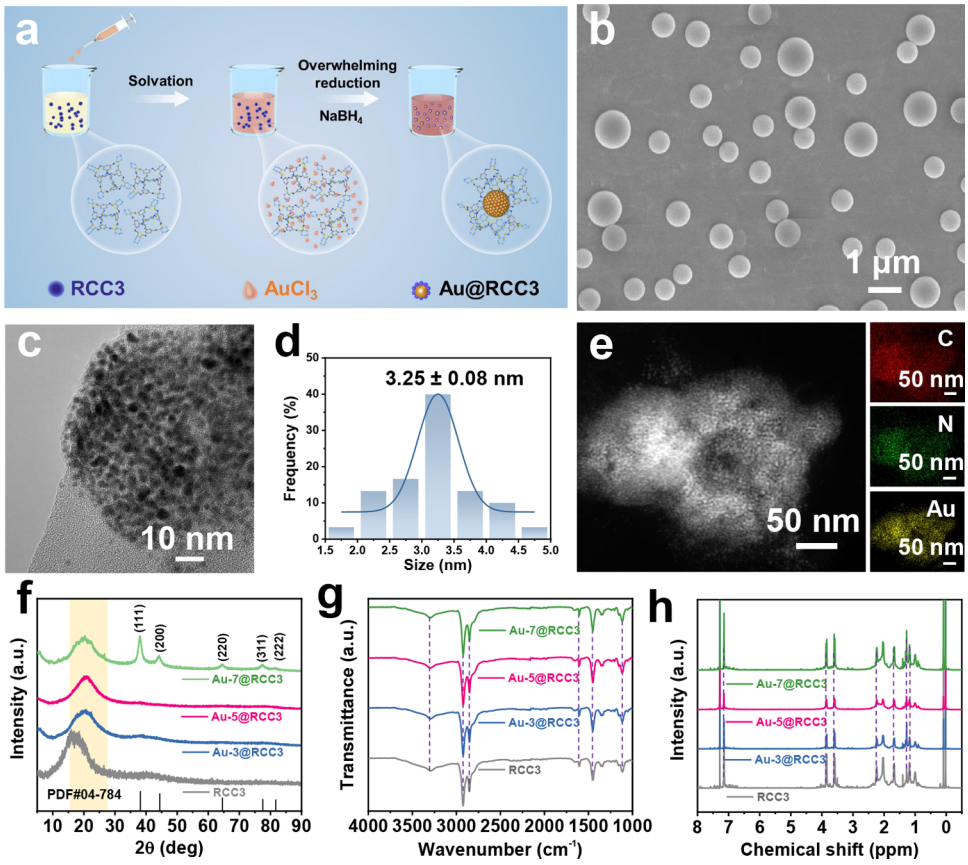

Figure 2. (a) Schematic illustration of the encapsulation of Au nanoparticles with RCC3 cage. (b) SEM and (c) TEM images of Au-5@RCC3. (d) Histogram of particle size distribution of Au-5@RCC3. (e) TEM and the corresponding EDS mappings of Au-5@RCC3. (f) XRD patterns, (g) FTIR spectra, and (h) NMR spectra of RCC3, Au-3@RCC3, Au-5@RCC3, and Au-7@RCC3.

3. RESULTS AND DISCUSSION

To clarify the importance of Au nanoparticles size with catalytic activity, five Au models with different sizes (Au_1, Au_{12}, Au_{18}, Au_{25}, and Au_{134}) were constructed and anchored on a catalytically inert surface, as shown in Figure 1a. Notably, large Au clusters (e.g., Au_{134} and Au_{25}) would result in severe nanoagglomeration due to the high surface energy in discrete Au atoms, as well as a dramatically confined number of active sites for any catalytic processes. This phenomenon can also be proven from the perspective of density functional theory (DFT) calculations,[38] where the corresponding density of states (DOS) values of unsupported metal species with different sizes are shown in Figure 1b. It was found that decreasing the size of metal species is beneficial for changing the continuous metal valence band into relatively discrete electronic states and positively shifting the Fermi energy level (ε_F). As a result, a smaller metal cluster can facilitate its chemisorption to the adsorbates, which is due to the strong interactions between the adsorbate's molecular orbitals and the s/d bands/states of metal clusters with abundant electron

https://doi.org/10.1021/acsanm.1c03859
ACS Appl. Nano Mater. 2022, 5, 1276−1283

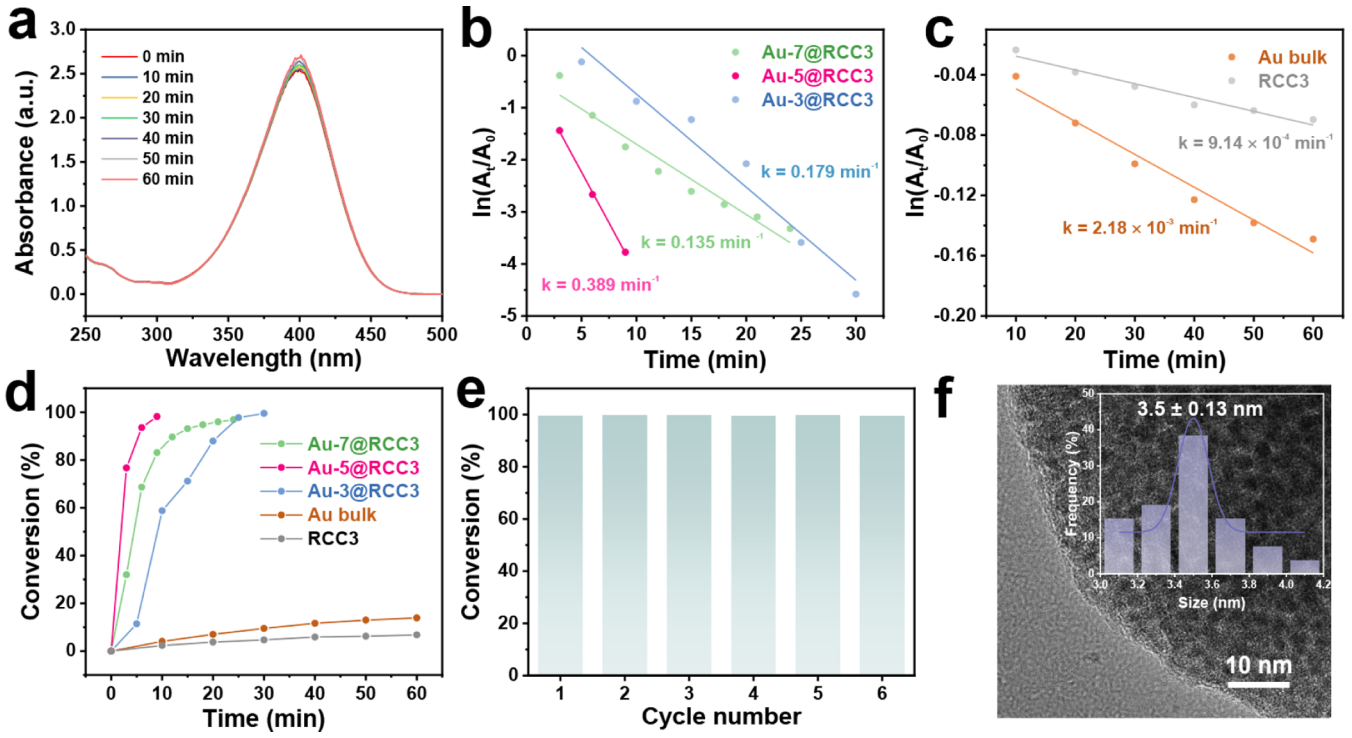

Figure 3. (a) UV−vis absorption spectra of 4-NP in CH_3OH/CH_2Cl_2 (v/v, 1/2) in the presence of $NaBH_4$ without catalyst. (b) Comparative catalytic conversion of 4-NP over various Au@RCC3 catalysts, Au bulk, and RCC3 at 298 K. (c) Plots of $\ln(A_t/A_0)$ of Au@RCC3 catalysts for the absorbance of 4-NP at 400 nm versus reaction time. (d) Plots of $\ln(A_t/A_0)$ of Au bulk and RCC3 for the absorbance of 4-NP at 400 nm versus reaction time. (e) Recyclability of Au-5@RCC3 during the hydrogenation of 4-NP at 298 K. (f) TEM image of Au-5@RCC3 after six cycles (inset: particle size distribution of Au nanoparticles).

transfer from metal clusters to the antibonding orbitals of adsorbates, resulting in an enhanced catalytic process. Therefore, it proves to be an ideal strategy to boost the catalytic activity of Au-based catalysts by reducing their particle size.[42,45]

The amine cage RCC3 formed by the reduction of imine cage CC3 (more synthetic details of CC3 and RCC3 are provided in Figure S1) was used to confine and stabilize ultrafine Au nanoparticles. The structural characterizations for CC3 (Figures S2−S6) and RCC3 (Figures S7−S13) are provided in the Supporting Information. Attributed to the good solubility of RCC3 in organic solvents, various Au@RCC3 composites with different amounts of Au nanoparticles can be well formed in a mixed solution of CH_3OH and CH_2Cl_2 (v/v, 1/2), as shown in Figures 2a and S14 (more details are provided in the Supporting Information). The solubility of Au@RCC3 with different Au loadings in the CH_3OH/CH_2Cl_2 (v/v, 1/2) solvent was tested at room temperature. It can be found that with the increase of Au loadings, the solubility of Au@RCC3 decreases (Figure S15). This shows that the dispersibility of Au@RCC3 in the solvent is affected by Au loadings. As the scanning electron microscopy (SEM) images of various Au@RCC3 composites show in Figures 2b and S16, the Au nanoparticles in RCC3 have negative effects on the spherical shape of RCC3 (Figure S12), where Au-5@RCC3 shows a uniform diameter distribution between 600 and 700 nm. The transmission electron microscopy (TEM) images of three Au@RCC3 (Figures 2c,d and S17) show that the average diameters of Au-3@RCC3, Au-5@RCC3, and Au-7@RCC3 are 2.9, 3.25, and 3.9 nm, respectively, which are all larger than the estimated pore size of the RCC3 cage (~0.7 nm).[48] It demonstrated that the Au nanoparticles are confined inside by several RCC3 cages instead of a single cage. Additionally, the energy-dispersive X-ray spectroscopy (EDS) elemental mappings (Figure 2e) and the corresponding EDS spectrum (Figure S18) of the Au-5@RCC3 composite further confirm the uniform distribution of Au inside RCC3 cages. The Au loadings in Au-3@RCC3, Au-5@RCC3, and Au-7@RCC3 composites are determined by thermogravimetric analysis (TGA, Figure S19) to be 2.43, 4.22, and 6.46 wt %, respectively. Through further analysis of TGA curves, we believe that Au@RCC3 composites can maintain good thermal stability in the air atmosphere below 300 °C without decomposition. The loadings of Au in three Au@RCC3 composites are also confirmed by the results from inductively coupled plasma emission spectrometry (Table S1). As the X-ray diffraction (XRD) patterns show in Figure 2f, various Au@RCC3 composites display broad peaks in the range of 10−30°, which are similar to the pattern of the RCC3 cage. Meanwhile, it is easy to observe the pattern of Au nanoparticles (JCPDS No. 04-784) in Au-7@RCC3, without the detection of the XRD pattern of Au nanoparticles in both Au-3@RCC3 and Au-5@RCC3. This may be due to the poor dispersion of Au agglomeration outside the molecular cage of RCC3 in Au-7@RCC3. However, no pronounced diffraction peaks appear in Au-3@RCC3 or Au-5@RCC3, demonstrating the excellent dispersion of confined Au nanoparticles inside the molecular cages. The Fourier transform infrared (FTIR) spectra of various Au@RCC3 composites are almost the same as those of the RCC3 cage (Figure 2g), suggesting that the encapsulation of Au nanoparticle does not destruct the covalent bonds of RCC3. The signals at 3300 and 1114 cm^{-1} indicate the existence of $-NH_2-$ and $-C-N-$, respectively. The signals at 2926 and 2852 cm^{-1} indicate the existence of $-CH_2-$, and the

https://doi.org/10.1021/acsanm.1c03859
ACS Appl. Nano Mater. 2022, 5, 1276−1283

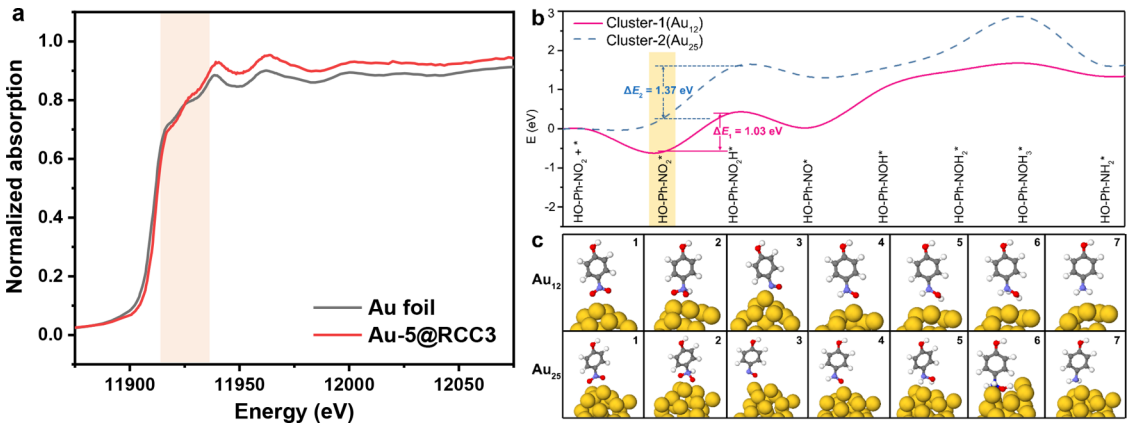

Figure 4. (a) Normalized XANES spectra at the Au L_3 edge of Au foil and Au-5@RCC3. (b) Hydrolysis mechanism of 4-NP to 4-AP on Au clusters of different sizes based on DFT calculations. The solid pink line shows the energetics with cluster-1 (Au_{12}), while the energetics with cluster-2 (Au_{25}) are shown as blue dotted lines. (c) Schematic diagram of the reaction pathways of 4-NP in Au_{12} and Au_{25} clusters.

signals at 1603 and 1448 cm^{-1} indicate the existence of −C=C− in the benzene ring. The structural preservations of RCC3 cages in various Au@RCC3 composites are also confirmed from their similar ^1H and ^{13}C nuclear magnetic resonance (NMR) spectra compared to that of RCC3 (Figures 2h and S20). The peaks appearing at 3.83 and 3.61 ppm are assigned to the hydrogen signals in $-CH_2-$ attached to the benzene ring. The peaks at 7.13, 2.23, and 0.95−1.98 ppm are assigned to the hydrogen signals in the benzene ring, cyclohexane, and $-CH_2-$ attached to cyclohexane, respectively. X-ray photoelectron spectroscopy (XPS) analysis confirms the existence of Au nanoparticles in Au-5@RCC3 with binding energies at 86.9 and 83.1 eV (Figure S21), corresponding to Au $4f_{5/2}$ and Au $4f_{7/2}$ of metal Au.[52]

To evaluate the catalytic activities of various Au@RCC3 composites, a hydrogenation reaction from 4-NP to 4-AP under a $NaBH_4$-contained liquid phase was selected and studied as an example. First, the reagent 4-NP solution shows a strong absorption peak at 317 nm from its ultraviolet−visible (UV−vis) absorption spectrum (Figure S22), which positively shifts to 400 nm after adding reductant of $NaBH_4$ and forming the 4-NP ion. The $NaBH_4$ cannot reduce 4-NP to 4-AP alone without the existence of Au@RCC3 catalyst. After adding a certain amount of Au@RCC3 catalyst, the color of the solution quickly changed from bright yellow to colorless with the diminishment of the intensity of the absorption peaks at 400 nm. At the same time, a newly emerging absorption peak caused by the reaction product 4-AP appears at 300 nm, which could be used to quantificationally determine the catalytic efficiency of various Au@RCC3 catalysts. The complete hydrogenations of 4-NP to 4-AP in the presence of Au-3@RCC3, Au-5@RCC3, and Au-7@RCC3 catalysts require 24, 9, and 30 min, respectively (Figure 3b). A linear correlation between $\ln(A_t/A_0)$ and reaction time can be obtained using a proposed first-stage kinetic model (A_t and A_0 represent the absorbances of the interval and the initial phase of 4-NP ion, respectively).[10−14] As shown in Figure 3c, the rate constant (k) of Au-5@RCC3 is 0.389 min^{-1}, which is higher than those of Au-7@RCC3 (k = 0.135 min^{-1}) and Au-3@RCC3 (k = 0.179 min^{-1}). Therefore, the Au-5@RCC3 catalyst has the best catalytic performance compared with the other two catalysts. This is because Au-5@RCC3 has a moderate loading of Au nanoparticles, which results in a larger number of active Au atoms (compared to Au-3@RCC3) and suppressive aggregation of Au nanoparticles (compared to Au-7@RCC3). Additionally, Au bulk was prepared as a counterpart with the corresponding morphology and structure characterizations in Figure S23. The diffraction peaks of Au bulk in the XRD pattern (Figure S23a) are sharp and consistent with the Au phase. The SEM image (Figure S23b) shows that Au particles in Au bulk agglomerate severely without the immobilization of the RCC3 cage. Au bulk with a large particle size becomes insoluble in the liquid phase, leading to a much lower k of Au bulk (2.18×10^{-3} min^{-1}) than the corresponding Au@RCC3 composites (Figure 3d). Additionally, the RCC3 cage displays a negative catalytic performance, which is only used to adsorb the reagents (Figure 3d). Comparing with the turnover frequency (TOF) values of Au@RCC3, Au bulk, and RCC3 (Table S2), we find that the TOF value of Au-5@RCC3 is approximately 47 times higher than that of Au bulk. Meanwhile, compared with the 4-NP reduction performance of other Au-based catalysts (Table S3), Au@RCC3 also has better catalytic performance. The stability and recyclability of Au-5@RCC3 are also examined using the reduction reaction of 4-NP. After being recycled six times, the Au-5@RCC3 catalyst still kept a high catalytic performance with stable activity (Figure 4e). The corresponding TEM image of the recovered material reveals that its average particle size (~3.5 nm) has increased slightly, which may be caused by the agglomeration of a tiny part of Au nanoparticles in Au-5@RCC3. These outcomes further approve that the finely dispersed Au nanoparticles are strongly attached to the porous architecture of organic cage and keep stable even after several catalytic cycles.

To unveil the primary cause of the enhanced catalysis in Au-5@RCC3, the electronic properties of the Au-5@RCC3 and Au foil (reference sample) were evaluated by X-ray absorption spectroscopy (XAS). The normalized X-ray absorption near-edge structure (XANES) of the Au L_3 edge for Au-5@RCC3 with the reference sample of Au foil is shown in Figure 4a. The white line intensity of Au-5@RCC3 is much higher than that of Au foil, indicating electron deficiency of the Au atoms in Au-5@RCC3 due to the small size of Au nanoparticles inside the RCC3 cage. As a result, the lightly oxidized Au species originating from the interaction between RCC3 and Au NPs play a positive role in the reduction of 4-NP,[53,54] which could be regarded as an electronic relay system to accelerate the

https://doi.org/10.1021/acsanm.1c03859
ACS Appl. Nano Mater. 2022, 5, 1276−1283

electron transfer from BH_4^- to 4-NP during hydrogenation,[54] resulting in the better catalytic performance of Au-5@RCC3.

Furthermore, the catalytic mechanism (size effect of Au nanoparticles) for the reduction of 4-NP in the presence of $NaBH_4$ was revealed by density functional theory (DFT) calculations on Au nanoparticles with different sizes, including Au_{12} as cluster-1 (Au_{12}) and Au_{25} as cluster-2 (Au_{25}). Despite the observation formation of the 4-NP ion during the experimental process, a protonated form of the phenolic group was applied for the following DFT calculations to maintain the neutrality of the simulated system.[55] As the reaction center is located at the functional group of NO_2, the deprotonated phenolic group has a negative effect relative to the energy expected. For the reduction reaction from 4-NP to 4-AP, there are six steps in total. In detail, the hydride (H^-) of $NaBH_4$ nucleophilically attacks the nitrogen atom to generate the NHO_2^- group as the first step. Then, 4-NP is generated after the dehydroxylation from the HNO_2^- group to the NO group. A second due to the strong Brønsted acidity of the HNO^- group, the NH_2O group of 4-hydroxyaminophenol is generated by the hydrolysis of the NHO^- group. After a third transfer of hydride from $NaBH_4$, the as-reduced intermediate of the NH_3O^- group is finally converted into the product of 4-AP by a further dehydroxylation process. For the two models of cluster-1 (Au_{12}) and cluster-2 (Au_{25}), the energy values for the above-mentioned steps are listed in Figure 4b and Table S4. In particular, the rate-determining steps for both cluster-1 (Au_{12}) and cluster-2 (Au_{25}) surfaces are the first transfer of hydride (HO-Ph-NO_2* → HO-Ph-NO_2H*) with energy barriers of 1.03 eV for cluster-1 (Au_{12}) and 1.37 eV for cluster-2 (Au_{25}). This significant energy difference between the two models indicates that the smaller nanoparticles favor hydride transfer for the reduction of 4-NP. This matches well with the prediction in Figure 1. This further indicates the importance of encapsulating MNPs with POCs to control their size and prevent clustering in the catalytic reaction.

4. CONCLUSIONS

In summary, we successfully confined ultrafine Au nanoparticles (~3.25 nm) inside porous organic cages to generate a Au-5@RCC3 nanocatalyst, which exhibits excellent catalytic reduction of 4-NP compared to that of Au bulk. The performance enhancement originates from the dramatically reduced size of Au nanoparticles and the good solubility of Au-5@RCC3 nanocatalyst in the reaction system, which can expose abundant active sites and facilitate the penetration of reagents during the catalytic process. As revealed by XANES results, the Au atoms in Au@RCC3 have been partially oxidized such that the electron-deficient state is beneficial for accelerating the electron transfer from BH_4^- to 4-NP during the hydrogenation process. The DFT calculations further demonstrate that a decreased size of Au nanoparticles is beneficial for the reduction of 4-NP, where the Au_{12} cluster shows a lower energy barrier of 1.03 eV compared with 1.37 eV for the Au_{25} cluster. Therefore, our work provides guidance for the rational design of novel and efficient noble-metal-based nanocatalysts using porous organic cages as a matrix to stabilize ultrafine metal nanoparticles uniformly.

■ ASSOCIATED CONTENT

Supporting Information

The Supporting Information is available free of charge at https://pubs.acs.org/doi/10.1021/acsanm.1c03859.

Characterizations; schematic illustration of the synthesis of the RCC3 cage; SEM image of CC3; ^{1}H NMR spectrum of CC3; XRD pattern of CC3; N_2 absorption/desorption isotherms of CC3, cumulative surface area, and (inset) pore size distribution of CC3; thermogravimetric analysis (TGA) profile of CC3; ^{1}H NMR spectrum of RCC3; ^{13}C NMR spectrum of RCC3; FTIR spectra of RCC3; XPS results of RCC3; XRD patterns of the RCC3 cage with CH_2Cl_2 and the desolvated RCC3; SEM image of RCC3; TEM image of RCC3; visual color change during the synthesis of Au-5@RCC3; solubility of Au@RCC3 in CH_3OH/CH_2Cl_2 (v/v, 1/2) solvents; SEM images of Au-3@RCC3, Au-5@RCC3 and Au-7@RCC3; TEM images and the corresponding particle size distribution of Au-3@RCC3 and Au-7@RCC3; the corresponding energy-dispersive spectrum (EDS) of Au-5@RCC3; TGA profiles of three Au@RCC3 catalysts and RCC3; ^{13}C NMR spectra of RCC3 and three Au@RCC3 catalysts; Au 4f XPS spectrum for Au-5@RCC3; UV−vis absorption spectrum of 4-NP in CH_2Cl_2/CH_3OH without $NaBH_4$ and any catalyst; XRD pattern of Au bulk and SEM image of Au bulk; catalytic hydrogenation of Au-7@RCC3; catalytic hydrogenation of Au-5@RCC3; catalytic hydrogenation of Au-3@RCC3; catalytic hydrogenation of Au bulk; catalytic hydrogenation of RCC3; UV−vis curves of 4-NP with known 4-NP ion concentration (Figures S1−S29); mass ratios of C, H, N, and Au in RCC3 and Au@RCC3 composites, TOF values of the catalysts for the hydrogenation reduction of 4-NP, the rate constant (k) of different catalysts for catalytic reduction of 4-NP, and DFT calculated reaction energetics of each reaction step (Tables S1−S4) (PDF)

■ AUTHOR INFORMATION

Corresponding Authors

Feili Lai − *Department of Chemistry, KU Leuven, Leuven 3001, Belgium;* orcid.org/0000-0002-4945-0737; Email: feili.lai@kuleuven.be

Tianxi Liu − *State Key Laboratory for Modification of Chemical Fibers and Polymer Materials, College of Materials Science and Engineering, Innovation Center for Textile Science and Technology, Donghua University, Shanghai 201620, P. R. China; Key Laboratory of Synthetic and Biological Colloids, Ministry of Education, School of Chemical and Material Engineering, International Joint Research Laboratory for Nano Energy Composites, Jiangnan University, Wuxi 214122, P. R. China*; Email: txliu@jiangnan.edu.cn

Authors

Yali Liu − *State Key Laboratory for Modification of Chemical Fibers and Polymer Materials, College of Materials Science and Engineering, Innovation Center for Textile Science and Technology, Donghua University, Shanghai 201620, P. R. China*

Hongliang Dong − *Center for High Pressure Science and Technology Advanced Research, Shanghai 201203, P. R. China*

Haowei Huang − *Department of Chemistry, KU Leuven, Leuven 3001, Belgium;* orcid.org/0000-0002-2901-8189

Wei Zong − *State Key Laboratory for Modification of Chemical Fibers and Polymer Materials, College of Materials*

Science and Engineering, Innovation Center for Textile Science and Technology, Donghua University, Shanghai 201620, P. R. China

Yue-E Miao − *State Key Laboratory for Modification of Chemical Fibers and Polymer Materials, College of Materials Science and Engineering, Innovation Center for Textile Science and Technology, Donghua University, Shanghai 201620, P. R. China;* orcid.org/0000-0002-3660-029X

Guanjie He − *Christopher Ingold Laboratory, Department of Chemistry, University College London, London WC1H 0AJ, U.K.;* orcid.org/0000-0002-7365-9645

Ivan P. Parkin − *Christopher Ingold Laboratory, Department of Chemistry, University College London, London WC1H 0AJ, U.K.;* orcid.org/0000-0002-4072-6610

Complete contact information is available at: https://pubs.acs.org/10.1021/acsanm.1c03859

Author Contributions

#Y.L. and H.D. contributed equally to this work. The manuscript was written through contributions of all of the authors. All of the authors have given approval to the final version of the manuscript.

Notes

The authors declare no competing financial interest.

■ ACKNOWLEDGMENTS

The authors are grateful for the financial support from the National Natural Science Foundation of China (21674019), the Natural Science Foundation of Shanghai (20ZR1401400), the Shanghai Scientific and Technological Innovation Project (18JC1410600), the Program of Shanghai Academic Research Leader (17XD1400100), and the Fundamental Research Funds for the Central Universities and DHU Distinguished Young Professor Program (LZB2021002). Theoretical work was carried out at the LvLiang Cloud Computing Center of China, and the calculations were performed on TianHe-2. The authors thank Y. Liu and Z. Zhang for their assistance and beamline 4B9A at the Beijing Synchrotron Radiation Facility (BSRF, Beijing, China).

■ REFERENCES

(1) Kong, X.; Sun, Z.; Chen, M.; Chen, C.; Chen, Q. Metal-free catalytic reduction of 4-nitrophenol to 4-aminophenol by N-doped graphene. *Energy Environ. Sci.* **2013**, *6*, 3260.

(2) Liu, X.; Wu, L.; Liu, T.; Zhang, L. In situ confine of Co_3ZnC/Co in N-doped carbon nanotube-grafted graphitic carbon nanoflakes as 1D-2D hierarchical catalysts toward superior redox activity. *Appl. Catal., B* **2021**, *281*, No. 119513.

(3) Chu, C.; Rao, S.; Ma, Z.; Han, H. Copper and cobalt nanoparticles doped nitrogen-containing carbon frameworks derived from CuO-encapsulated ZIF-67 as high-efficiency catalyst for hydrogenation of 4-nitrophenol. *Appl. Catal., B* **2019**, *256*, No. 117792.

(4) Malengreaux, C. M.; Pirard, S. L.; Bartlett, J. R.; Heinrichs, B. Kinetic study of 4-nitrophenol photocatalytic degradation over a Zn^{2+} doped TiO_2 catalyst prepared through an environmentally friendly aqueous sol-gel process. *Chem. Eng. J.* **2014**, *245*, 180−190.

(5) Hasan, Z.; Cho, D.; Chon, C.; Yoon, K.; Song, H. Reduction of p-nitrophenol by magnetic Co-carbon composites derived from metal organic frameworks. *Chem. Eng. J.* **2016**, *298*, 183−190.

(6) Liu, Q.; Zheng, T.; Wang, P.; Jiang, J.; Li, N. Adsorption isotherm, kinetic and mechanism studies of some substituted phenols on activated carbon fibers. *Chem. Eng. J.* **2010**, *157*, 348−356.

(7) Ren, L.; Yi, X.; Tong, L.; Zhou, W.; Wang, D.; Liu, L.; Ye, J. Nitrogen-doped ultrathin graphene encapsulated Cu nanoparticles decorated on $SrTiO_3$ as an efficient water oxidation photocatalyst with activity comparable to $BiVO_4$ under visible-light irradiation. *Appl. Catal., B* **2020**, *279*, No. 119352.

(8) Martin-Martinez, M.; Barreiro, M. F. F.; Silva, A. M. T.; Figueiredo, J. L.; Faria, J. L.; Gomes, H. T. Lignin-based activated carbons as metal-free catalysts for the oxidative degradation of 4-nitrophenol in aqueous solution. *Appl. Catal., B* **2017**, *219*, 372−378.

(9) Xu, Y.; Shi, X.; Hua, R.; Zhang, R.; Yao, Y.; Zhao, B.; Liu, T.; Zheng, J.; Lu, G. Remarkably catalytic activity in reduction of 4-nitrophenol and methylene blue by Fe_3O_4@COF supported noble metal nanoparticles. *Appl. Catal., B* **2020**, *260*, No. 118142.

(10) Lu, S.; Hu, Y.; Wan, S.; McCaffrey, R.; Jin, Y.; Gu, H.; Zhang, W. Synthesis of Ultrafine and Highly Dispersed Metal Nanoparticles Confined in a Thioether-Containing Covalent Organic Framework and Their Catalytic Applications. *J. Am. Chem. Soc.* **2017**, *139*, 17082−17088.

(11) Tao, R.; Shen, X.; Hu, Y.; Kang, K.; Zheng, Y.; Luo, S.; Yang, S.; Li, W.; Lu, S.; Jin, Y.; et al. Phosphine-Based Covalent Organic Framework for the Controlled Synthesis of Broad-Scope Ultrafine Nanoparticles. *Small* **2020**, *16*, No. 1906005.

(12) He, Z.; Liu, R.; Xu, C.; Lai, Y.; Shan, W.; Liu, J. Black phosphorus hybridizing produces electron-deficient active sites on palladium nanoparticles for catalysis. *Appl. Catal., B* **2021**, *285*, No. 119775.

(13) Sun, N.; Wang, C.; Wang, H.; Yang, L.; Jin, P.; Zhang, W.; Jiang, J. Multifunctional Tubular Organic Cage-Supported Ultrafine Palladium Nanoparticles for Sequential Catalysis. *Angew. Chem., Int. Ed.* **2019**, *58*, 18011−18016.

(14) Lawrence, R. L.; Scola, B.; Li, Y.; Lim, C.; Liu, Y.; Prasad, P. N.; Swihart, M. T.; Knecht, M. R. Remote Optically Controlled Modulation of Catalytic Properties of Nanoparticles through Reconfiguration of the Inorganic/Organic Interface. *ACS Nano* **2016**, *10*, 9470−9477.

(15) Chen, P.; Liu, G.; Zhou, Y.; Brown, K. A.; Chernyak, N.; Hedrick, J. L.; He, S.; Xie, Z.; Lin, Q.; Dravid, V. P.; et al. Tip-Directed Synthesis of Multimetallic Nanoparticles. *J. Am. Chem. Soc.* **2015**, *137*, 9167−9173.

(16) Lu, Y.; Yuan, J.; Polzer, F.; Drechsler, M.; Preussner, J. In Situ Growth of Catalytic Active Au-Pt Bimetallic Nanorods in Thermoresponsive Core-Shell Microgels. *ACS Nano* **2010**, *4*, 7078−7086.

(17) Deng, Y.; Cai, Y.; Sun, Z.; Liu, J.; Liu, C.; Wei, J.; Li, W.; Liu, C.; Wang, Y.; Zhao, D. Multifunctional Mesoporous Composite Microspheres with Well-Designed Nanostructure: A Highly Integrated Catalyst System. *J. Am. Chem. Soc.* **2010**, *132*, 8466−8473.

(18) Qi, H.; Yu, P.; Wang, Y.; Han, G.; Liu, H.; Yi, Y.; Li, Y.; Mao, L. Graphdiyne Oxides as Excellent Substrate for Electroless Deposition of Pd Clusters with High Catalytic Activity. *J. Am. Chem. Soc.* **2015**, *137*, 5260−5263.

(19) Weng, B.; Jiang, Y.; Liao, H.; Roeffaers, M. B. J.; Lai, F.; Huang, H.; Tang, Z. Visualizing light-induced dynamic structural transformations of Au clusters-based photocatalyst via in situ TEM. *Nano Res.* **2021**, *14*, 2805−2809.

(20) Zhu, Y.; Fan, L.; Yang, B.; Du, J. Multifunctional Homopolymer Vesicles for Facile Immobilization of Gold Nanoparticles and Effective Water Remediation. *ACS Nano* **2014**, *8*, 5022−5031.

(21) Sun, L.; Zhang, Q.; Li, G. G.; Villarreal, E.; Fu, X.; Wang, H. Multifaceted Gold-Palladium Bimetallic Nanorods and Their Geometric, Compositional, and Catalytic Tunabilities. *ACS Nano* **2017**, *11*, 3213−3228.

(22) Hu, J.; Yang, Q.; Yang, L.; Zhang, Z.; Su, B.; Bao, Z.; Ren, Q.; Xing, H.; Dai, S. Confining Noble Metal (Pd, Au, Pt) Nanoparticles in Surfactant Ionic Liquids: Active Non-Mercury Catalysts for Hydrochlorination of Acetylene. *ACS Catal.* **2015**, *5*, 6724−6731.

(23) Zhong, R.; Sun, K.; Hong, Y.; Xu, B. Impacts of Organic Stabilizers on Catalysis of Au Nanoparticles from Colloidal Preparation. *ACS Catal.* **2014**, *4*, 3982−3993.

(24) Wang, Y.; Wan, X.; Ren, L.; Su, H.; Li, G.; Malola, S.; Lin, S.; Tang, Z.; Häkkinen, H.; Teo, B. K.; et al. Atomically Precise Alkynyl-Protected Metal Nanoclusters as a Model Catalyst: Observation of Promoting Effect of Surface Ligands on Catalysis by Metal Nanoparticles. *J. Am. Chem. Soc.* **2016**, *138*, 3278−3281.
(25) Fan, Y.; Xiao, H.; Shi, G.; Liu, H.; Bao, X. A novel approach for modulating the morphology of supported metal nanoparticles in hydrodesulfurization catalysts. *Energy Environ. Sci.* **2011**, *4*, 572−582.
(26) Chao, G.; Zhang, L.; Tian, J.; Fan, W.; Liu, T. Pd-SnO_2 heterojunction catalysts anchored on graphene sheets for enhanced oxygen reduction. *Compos. Commun.* **2021**, *25*, No. 100703.
(27) Chao, G.; An, X.; Zhang, L.; Tian, J.; Fan, W.; Liu, T. Electron-rich platinum electrocatalysts supported onto tin oxides for efficient oxygen reduction. *Compos. Commun.* **2021**, *24*, No. 100603.
(28) Tozawa, T.; Jones, J. T.; Swamy, S. I.; Jiang, S.; Adams, D. J.; Shakespeare, S.; Clowes, R.; Bradshaw, D.; Hasell, T.; Chong, S.; Tang, C.; Thompson, S.; Parker, J.; Trewin, A.; Bacsa, J.; Slawin, A. M.; Steiner, A.; Cooper, A. I. Porous Organic Cages. *Nat. Mater.* **2009**, *8*, 973−978.
(29) Avellaneda, A.; Valente, P.; Burgun, A.; Evans, J. D.; Markwell-Heys, A. W.; Rankine, D.; Nielsen, D. J.; Hill, M. R.; Sumby, C. J.; Doonan, C. J. Kinetically Controlled Porosity in a Robust Organic Cage Material. *Angew. Chem., Int. Ed.* **2013**, *52*, 3746−3749.
(30) Wang, H.; Jin, Y.; Sun, N.; Zhang, W.; Jiang, J. Post-synthetic modification of porous organic cages. *Chem. Soc. Rev.* **2021**, *50*, 8874−8886.
(31) Huang, S.; Lei, Z.; Jin, Y.; Zhang, W. By-design molecular architectures via alkyne metathesis. *Chem. Sci.* **2021**, *12*, 9591−9606.
(32) Acharyya, K.; Mukherjee, P. S. Organic Imine Cages: Molecular Marriage and Applications. *Angew. Chem.* **2019**, *131*, 8732−8745.
(33) Liu, M.; Zhang, L.; Little Marc, A.; Kapil, V.; Ceriotti, M.; Yang, S.; Ding, L.; Holden Daniel, L.; Balderas-Xicohténcatl, R.; He, D.; Clowes, R.; Chong Samantha, Y.; Schütz, G.; Chen, L.; Hirscher, M.; Cooper, A. I. Barely porous organic cages for hydrogen isotope separation. *Science* **2019**, *366*, 613−620.
(34) Hasell, T.; Miklitz, M.; Stephenson, A.; Little, M. A.; Chong, S. Y.; Clowes, R.; Chen, L.; Holden, D.; Tribello, G. A.; Jelfs, K. E.; et al. Porous Organic Cages for Sulfur Hexafluoride Separation. *J. Am. Chem. Soc.* **2016**, *138*, 1653−1659.
(35) Chen, L.; Reiss, P. S.; Chong, S. Y.; Holden, D.; Jelfs, K. E.; Hasell, T.; Little, M. A.; Kewley, A.; Briggs, M. E.; Stephenson, A.; Thomas, K. M.; Armstrong, J. A.; Bell, J.; Busto, J.; Noel, R.; Liu, J.; Strachan, D. M.; Thallapally, P. K.; Cooper, A. I. Separation of rare gases and chiral molecules by selective binding in porous organic cages. *Nat. Mater.* **2014**, *13*, 954−960.
(36) Brutschy, M.; Schneider, M. W.; Mastalerz, M.; Waldvogel, S. R. Porous Organic Cage Compounds as Highly Potent Affinity Materials for Sensing by Quartz Crystal Microbalances. *Adv. Mater.* **2012**, *24*, 6049−6052.
(37) Wang, Z.; Ma, H.; Zhai, T. L.; Cheng, G.; Xu, Q.; Liu, J. M.; Yang, J. K.; Zhang, Q. M.; Zhang, Q. P.; Zheng, Y. S.; Tan, B.; Zhang, C. Networked Cages for Enhanced CO_2 Capture and Sensing. *Adv. Sci.* **2018**, *5*, No. 1800141.
(38) Jin, Y.; Voss, B. A.; McCaffrey, R.; Baggett, C. T.; Noble, R. D.; Zhang, W. Microwave-assisted syntheses of highly CO_2-selective organic cage frameworks (OCFs). *Chem. Sci.* **2012**, *3*, 874−877.
(39) Zhu, Q.; Wang, X.; Clowes, R.; Cui, P.; Chen, L.; Little, M. A.; Cooper, A. I. 3D Cage COFs: A Dynamic Three-Dimensional Covalent Organic Framework with High-Connectivity Organic Cage Nodes. *J. Am. Chem. Soc.* **2020**, *142*, 16842−16848.
(40) Little, M. A.; Chong, S. Y.; Schmidtmann, M.; Hasell, T.; Cooper, A. I. Guest control of structure in porous organic cages. *Chem. Commun.* **2014**, *50*, 9465−9468.
(41) Wang, Z.; Reddy, C. B.; Zhou, X.; Ibrahim, J. J.; Yang, Y. Phosphine-Built-in Porous Organic Cage for Stabilization and Boosting the Catalytic Performance of Palladium Nanoparticles in Cross-Coupling of Aryl Halides. *ACS Appl. Mater. Interfaces* **2020**, *12*, 53141−53149.
(42) McCaffrey, R.; Long, H.; Jin, Y.; Sanders, A.; Park, W.; Zhang, W. Template Synthesis of Gold Nanoparticles with an Organic Molecular Cage. *J. Am. Chem. Soc.* **2014**, *136*, 1782−1785.
(43) Qiu, L.; McCaffrey, R.; Jin, Y.; Gong, Y.; Hu, Y.; Sun, H.; Park, W.; Zhang, W. Cage-templated synthesis of highly stable palladium nanoparticles and their catalytic activities in Suzuki-Miyaura coupling. *Chem. Sci.* **2018**, *9*, 676−680.
(44) Sun, J.; Zhan, W.; Akita, T.; Xu, Q. Toward Homogenization of Heterogeneous Metal Nanoparticle Catalysts with Enhanced Catalytic Performance: Soluble Porous Organic Cage as a Stabilizer and Homogenizer. *J. Am. Chem. Soc.* **2015**, *137*, 7063−7066.
(45) Mondal, B.; Mukherjee, P. S. Cage Encapsulated Gold Nanoparticles as Heterogeneous Photocatalyst for Facile and Selective Reduction of Nitroarenes to Azo Compounds. *J. Am. Chem. Soc.* **2018**, *140*, 12592−12601.
(46) Qiu, L.; McCaffrey, R.; Zhang, W. Synthesis of Metallic Nanoparticles Using Closed-Shell Structures as Templates. *Chem.—Asian J.* **2018**, *13*, 362−372.
(47) Hasell, T.; Zhang, H.; Cooper, A. I. Solution-Processable Molecular Cage Micropores for Hierarchically Porous Materials. *Adv. Mater.* **2012**, *24*, 5732−5737.
(48) Liu, M.; Little, M. A.; Jelfs, K. E.; Jones, J. T. A.; Schmidtmann, M.; Chong, S. Y.; Hasell, T.; Cooper, A. I. Acid- and Base-Stable Porous Organic Cages: Shape Persistence and pH Stability via Post-synthetic "Tying" of a Flexible Amine Cage. *J. Am. Chem. Soc.* **2014**, *136*, 7583−7586.
(49) Kresse, G.; Furthmuller, J. Efficient iterative schemes for ab initio total-energy calculations using a plane-wave basis set. *Phys. Rev. B* **1996**, *54*, 11169−11186.
(50) Blöchl, P. E. Projector augmented-wave method. *Phys. Rev. B* **1994**, *50*, 17953−17979.
(51) Perdew, J. P.; Burke, K.; Ernzerhof, M. Generalized Gradient Approximation Made Simple. *Phys. Rev. Lett.* **1996**, *77*, 3865−3868.
(52) Li, H.; Bian, Z.; Zhu, J.; Huo, Y.; Li, H.; Lu, Y. Mesoporous Au/TiO_2 Nanocomposites with Enhanced Photocatalytic Activity. *J. Am. Chem. Soc.* **2007**, *129*, 4538−4539.
(53) Zhang, J.; Chen, G.; Chaker, M.; Rosei, F.; Ma, D. Gold nanoparticle decorated ceria nanotubes with significantly high catalytic activity for the reduction of nitrophenol and mechanism study. *Appl. Catal., B* **2013**, *132*−*133*, 107−115.
(54) Fu, Y.; Huang, T.; Jia, B.; Zhu, J.; Wang, X. Reduction of nitrophenols to aminophenols under concerted catalysis by Au/g-C_3N_4 contact system. *Appl. Catal., B* **2017**, *202*, 430−437.
(55) Zhang, W.; Lu, G.; Cui, C.; Liu, Y.; Li, S.; Yan, W.; Xing, C.; Chi, Y. R.; Yang, Y.; Huo, F. A Family of Metal-Organic Frameworks Exhibiting Size-Selective Catalysis with Encapsulated Noble-Metal Nanoparticles. *Adv. Mater.* **2014**, *26*, 4056−4060.

https://doi.org/10.1021/acsanm.1c03859
ACS Appl. Nano Mater. 2022, 5, 1276−1283